# Mirage Sources and Large TeV Halo-Pulsar Offsets: Exploring the Parameter Space

Yiwei Bao<sup>1,2</sup>, Ruo-Yu Liu<sup>1,3</sup>,\* Gwenael Giacinti<sup>2,4</sup>,† Hai-Ming Zhang<sup>1</sup>, and Yang Chen<sup>1,3‡</sup>

<sup>1</sup>Department of Astronomy, Nanjing University, 163 Xianlin Avenue, Nanjing 210023, China

<sup>2</sup>Tsung-Dao Lee Institute, Shanghai Jiao Tong University, Shanghai 201210, China

<sup>3</sup>Key Laboratory of Modern Astronomy and Astrophysics,

Nanjing University, Ministry of Education, Nanjing, China

<sup>4</sup>School of Physics and Astronomy, Shanghai Jiao Tong University, Shanghai 200240, China

(Dated: July 4, 2024)

We investigate the asymmetric propagation of 100 TeV electrons (whose radiation mainly concentrates on 20–30 TeV) in turbulent magnetic fields around pulsars, using GPU-accelerated simulations to explore their trajectories and interactions within pulsar wind nebulae and the interstellar medium. Key results include the identification of "mirage" sources indicating significant offsets in high-energy emissions from their originating pulsars, challenging the results of traditional symmetric diffusion models. By varying parameters like source distance, magnetic field strength, and electron injection spectral index, the study delineates their effects on observable phenomena such as the probability that a source has at least one mirage around it, as well as the source separation. Our results offer insights into some puzzling sources observed recently by the Large High Altitude Air Shower Observatory (LHAASO), and shed light on the cosmic-ray transport mechanism in the interstellar medium.

## I. INTRODUCTION

Pulsars are rapidly rotating neutron stars. They power relativistic pulsar winds composed of  $e^{\pm}$  pairs [1–3] at the expense of their rotational energies. A termination shock is formed where the pulsar wind encounters the ambient medium and reaches a pressure balance. Either at the termination shock [4], or far upstream of the termination shock [5], magnetic reconnection may occur and some of the  $e^{\pm}$  pairs be accelerated up to  $\sim$  PeV [3]. Alternatively, these particles may be accelerated at the termination shock, especially in its equatorial region [6, 7]. The radiation of these relativistic pairs in the shocked wind gives rise to the pulsar wind nebula (PWN).

Recent observations of extended TeV emissions around middle-aged pulsars by HAWC [8] and LHAASO [9] have sparked significant interest among the community. It can be inferred from the surface brightness profiles of these extended  $\gamma$ -ray emission that  $e^{\pm}$  pairs are escaping their PWNe and diffusing in the ambient interstellar medium (ISM) with a significantly suppressed diffusion coefficient, by a factor of  $\sim 100 - 1000$ , compared to the Galactic mean value. It may be interpreted as an enhancement of the interstellar turbulence [10–12], or a reasonably large level of pre-existing turbulence [13], or ascribed to the cross-field transport of particles if the local magnetic field and the observer's line of sight is approximately aligned [14]. The size of the region with suppressed particle diffusion is suggested to be at least 20 pc [15]. The extended  $\gamma$ -ray emission region beyond the PWN is usually referred to as "TeV halos".

In principle, each middle-aged pulsar could power a

TeV halo [16, 17]. Indeed, we see many sources identified by LHAASO [18] and HAWC [19] are associated with middle-aged pulsars. However, many of them present significant spatial offsets between positions of the pulsars and the centroid of the TeV sources, which is not expected if pairs are injected from the position of the pulsar (or from the compact PWN around the pulsar) and isotropically diffuse in the surrounding ISM [20]. Actually, isotropic diffusion is a good approximation of the real transport of particles only if the physical scale considered in the problem is larger than multiple coherence lengths of the turbulent magnetic field [21] (about 1/5 of the outer scale of the turbulence for Kolmogorov spectra), such as e.g. in the modelling of the global transport of cosmic rays (CRs) in the Galaxy.

However, if we focus on the particle transport around accelerators, especially those located above/below the Galactic disk or in the outer Galaxy region, the isotropic diffusion approximation could be problematic, given that the average coherent length of the ISM is of the order of  $\sim 100\,\mathrm{pc}$  [22]. This is particularly important for pulsar halo candidates detected by LHAASO-KM2A, because these sources are due to the emission from electrons/positrons with energies above 100 TeV. Given the rapid cooling rate of these extremely energetic leptons, they may probably cool down before crossing one magnetic coherence length. Therefore, the distribution of high-energy particles could be highly asymmetric, following the direction of the local magnetic field. In the companion paper [23] (Paper I), we have shown that the asymmetric propagation of electrons/positrons around their accelerators may cause multiple "mirage" sources and significant spatial offset between the accelerator and the source. The main goal of the present paper is to give a more quantitative description of our method, and to explore extensively the influence of different model parameters on the obtained source morphology.

<sup>\*</sup> rvliu@nju.edu.cn

<sup>†</sup> gwenael.giacinti@sjtu.edu.cn

<sup>&</sup>lt;sup>‡</sup> ygchen@nju.edu.cn

The rest of the paper is organized as follows: in Section II, we describe our method in detail; we explore the properties of the simulated sources with different parameters in Section III; In Section IV, we discuss several possible applications of our findings, and we conclude in Section V.

## II. METHOD DESCRIPTION

To characterise the asymmetric propagation of particles, we conduct test-particle simulations by calculating the trajectories of 100 TeV electrons, the radiation spectrum of which typically peaks at approximately 20 TeV via the inverse Compton (IC) scattering off the cosmic microwave background (CMB). We employ a firstprinciple approach by injecting electrons into a turbulent magnetic field and determining their motion based on the Lorentz force [24–26]. We employ GPU-acceleration methods, allowing the code to operate in a highly parallelized manner. To preserve GPU on-board memory, we calculate the magnetic field anew at every time step for every particles' position. While this approach is timeintensive, it offers a greater accuracy compared to the method which specifies fields on a discrete spatial lattice in advance and interpolates while computing. Here, we thoroughly explain in detail the process of conducting the simulation in terms of particle motion and field generation.

## A. Turbulent magnetic fields

We follow the same method in Ref.[24] to generate the turbulent magnetic field. The field is written as a superposition of  $N_m$  plane waves with

$$B_{\mathbf{t}}(\mathbf{r}) = \sum_{n=1}^{N_m} A_n \epsilon_n \exp(i\mathbf{k}_n \cdot \mathbf{r} + i\beta_n), \tag{1}$$

where the explanation of  $A_n$ ,  $\epsilon_n$ , k and  $\beta_n$  can be found in [24]. In addition, in the formula

$$A^{2}(k_{n}) = \sigma^{2}G(k_{n}) \left[ \sum_{n=1}^{N_{m}} G(k_{n}) \right]^{-1},$$
 (2)

we use  $G(k_n) \propto k^{-5/3} \Delta k$  instead of the one used in [24]. Technically, a value of 100 waves per decade [see e.g., 25] is used to balance the speed and accuracy. In practice, we generate the random constants on CPU which determine the turbulent magnetic field and store them in the "constant memory" of GPU to accelerate the computation. There are 600 waves in total, which covers a range of 6 magnitudes. We have calculated 100 distinct configurations of the turbulent magnetic field and show a subset of these configurations, which exhibit intriguing properties.  $T_{\rm age}$ , the age of the pulsar, is adopted to be 110 kyr.

## B. Energy losses

For the synchrotron loss (in terms of  $\gamma$ ), we utilize

$$\dot{\gamma}_{\text{sync}} = -3.25 \times 10^{-8} \frac{B^2}{8\pi} \gamma^2,$$
 (3)

where B is the magnetic field strength (here we use  $B^2 = B_r^2 + B_t^2$ , where  $B_r$  is the regular component and  $B_t$  the root mean square of the turbulent component). For IC losses we use the approximation given by Fang et al. [27]:

$$\dot{\gamma}_{\rm IC} = -\frac{20c\sigma_{\rm T}\omega\gamma^2}{\pi^4 m_e c^2} Y(\gamma, T),\tag{4}$$

where  $\omega$  is the grey-body energy density, T the grey-body temperature and  $Y(\gamma,T)$  the parameterised approximation function [27]. For the IC seed photons, we use the interstellar radiation field averaged over a 2 kpc region surrounding the Sun as a reference, which is composed of five gray-body components with temperatures of 23209 K, 6150.4 K, 3249.3 K, 313.3 K, and 33.1 K [27]. These components have corresponding energy densities of 0.12, 0.23, 0.37, 0.055, and 0.25 eV cm<sup>-3</sup> [27], respectively.

#### C. Particle motions

We employ the original Boris pusher which avoids the phase error [see e.g., Boris A pusher in 28] to preserve phase space volume. Since the electric field in the turbulent plasma may be neglected [24], the Boris pusher can be written as

$$\mathbf{x}' := \mathbf{x}_{n-1} + \frac{1}{2}\mathbf{v}_{n-1} \cdot \Delta t \tag{5}$$

$$\boldsymbol{t} := \tan \frac{\theta}{2} \hat{\boldsymbol{b}} \tag{6}$$

$$\gamma \mathbf{v}' := \gamma \mathbf{v}_{n-1} + \gamma \mathbf{v}_{n-1} \times \mathbf{t} \tag{7}$$

$$\gamma \boldsymbol{v}_n = \gamma \boldsymbol{v}' + \frac{2}{1 + |\boldsymbol{t}|^2} \left( \gamma \boldsymbol{v}' \times \boldsymbol{t} \right)$$
 (8)

$$\boldsymbol{x}_n = \boldsymbol{x}' + \frac{1}{2}\boldsymbol{v}_n \cdot \Delta t \tag{9}$$

where  $\hat{\boldsymbol{b}} := \boldsymbol{B}/|\boldsymbol{B}|$  is the unit vector,  $\gamma$  the electron Lorenzz factor, n the time step,  $\boldsymbol{x}'$ ,  $\boldsymbol{t}$ ,  $\boldsymbol{v}'$  are three intermediate variables. A time step of 1/100 gyration period is utilized in the simulation. We also take synchrotron/IC losses into consideration. The spin-down luminosity of the pulsar is  $L(t) = L_0/[1+(t/\tau_0)^2]$ , where  $L_0$  is the initial spin-down luminosity and  $\tau_0$  the initial spin-down timescale. Electrons are injected in a power-law form as  $\mathrm{d}N/\mathrm{d}\gamma \propto \gamma^{-\alpha}$ , where  $\alpha$  the power-law index. To mimic the continuous injection of electrons, we inject  $\approx 10^4$  numerical particles continuously over time with energy  $\gamma(t_{\rm inj}) = \int_{t_{\rm age}}^{t_{\rm inj}} [\dot{\gamma}_{\rm sync}(\gamma) + \dot{\gamma}_{\rm IC}(\gamma)] + 100\,\mathrm{TeV}/m_ec^2$  so that all of them are cooled down to 100 TeV at time  $t_{\rm age}$ , where  $t_{\rm inj}$  is the injection time of the particle and  $t_{\rm age}$  the current age of pulsar. The value of  $t_{\rm inj}$  is set such that every

numerical particle represents roughly the same number of real electrons.

### III. SIMULATION DATA ANALYSIS

### A. Methods

To mimic observations, we envisage that the halo is measured by LHAASO-KM2A, the point spread function (PSF) of which can be approximated as a 2D Gaussian function with the standard deviation  $\sigma = 0.3^{\circ}$  around 20 TeV [29]. To present the simulation result more conveniently, we consider the measurement of the pulsar halo solely at 20 TeV and set a reference luminosity of the pulsar halo to be  $L_{\rm ref} = 6 \times 10^{32} \, \rm erg/s$  at this energy. This luminosity is about 6 times that of the observed luminosity of Geminga's halo in the range of  $8 - 40 \,\text{TeV}$  [8], which is not unreasonable. We choose this high value in order to make the relevant features of simulated pulsar halos more significant. According to LHAASO's effective area, the reference luminosity corresponds to a total event rate of  $1.6 \times 10^6 (250 \,\mathrm{pc}/d)^2$  counts per year for our reference scenario, where d is the distance of the pulsar to us. We set our region of interest (ROI) to a region with projected size of  $100 \,\mathrm{pc} \times 100 \,\mathrm{pc}$ . For the case of  $L_c = 400$  pc or d = 6 kpc, we use a ROI of  $400\,\mathrm{pc}\times400\,\mathrm{pc}$ . In any case, the ROI is divided into many elementary bins of  $0.1^{\circ} \times 0.1^{\circ}$  or correspondingly  $0.436 \,\mathrm{pc}(d/250 \,\mathrm{pc}) \times 0.436 \,\mathrm{pc}(d/250 \,\mathrm{pc})$ . We then can calculate the expected event count number in each bin based on the simulated intensity distribution of the pulsar halo.

To mimic the background, we generate a Poisson noise map (noise A) based on the background event rate measured from the Crab Nebula region, which is 1 event per hour within a 1° cone [3], or 0.318 count/hour in each bin. We then add the count number of the noise to the event number in each bin so that we obtain a simulated counts map. We then generate the model, composed of another Poisson noise (noise B) based on the measured background rate and a symmetrical 2D Gaussian template (with the normalisation, extension, and positron free) to fit the obtained counts map, and calculate the test statistic (TS) value (TS1) [8, 29]. If the TS value exceeds 25, we deem that we identify one source. Next, we set a model composed of noise B plus two symmetrical 2D Gaussian template to fit the obtained counts map again, and calculate the TS value (TS2). If TS2 exceeds TS1 by 25, we deem that we identify two sources. The chain continues by adding another hypothetical source until the increment of TS value is less than 25. Practically, we would identify one or two sources in most cases, and in a few cases more mirage sources may be also found in the identification process. In Figure 1 and Figure 2, we show four configurations of mirage sources and four of large offsets, respectively, for reference. In all panels in these two Figures, the electrons are injected at (0,0), in the center. The colors show the level of the relative

gamma-ray intensity as calculated from our simulations. In Figure 1, the black, green and orange dots correspond to the locations of the sources we detect. One can see that, in each panel, two more sources are detected far from the actual astrophysical source. These are mirage sources. In Figure 2, the green dots display the locations of the detected sources. In each panel, a considerable offset is clearly visible.

The formation of mirage sources is related to the magnetic field geometry. After escaping accelerators, electrons spiral around extensive magnetic field lines in the surrounding medium. They are scattered by irregularities in the magnetic field but their trajectories roughly follow the mean direction of the magnetic field over one coherence length  $L_{\rm c}$ . By definition, the mean field direction changes dramatically in another coherence length. If the field line within certain coherence length roughly orients with our line of sight, a visual projection effect leads to the apparent enhancement of electron column density in that direction, which is not necessarily toward the injection point, creating a mirage source or an offset. Note that the turbulent magnetic field is treated as the superposition of many plane waves. Therefore, apart from the main field direction change at the scale of  $\sim L_{\rm c}$ , there are also smaller bents in the magnetic field within one coherence length. Even if particles do not cross over one coherence length before cooling, they may still form mirage sources or offset due to these small bents.

### B. Mirage Ratio

Because magnetic fields are generated randomly, the resulting morphology of the pulsar halo and properties of the emission in one run can be quite different from another. Therefore, we need to study the problem in a statistical way. One relevant issue is how likely we would identify multiple sources around an accelerator (i.e., pulsar/pulsar wind nebula). This can be assessed with what we will call the "mirage ratio", defined here as the fraction of all runs with more than one sources identified in the mock data. We run the simulation with 100 randomly generated magnetic field configurations, and then measure the mirage ratio, denoted by  $\xi$ . We also vary parameters such as pulsar distance d, injection power-law indices  $\alpha$ ,  $B_{\rm r}/B_{\rm t}$  and  $B^2$  one by one to see their influences. The luminosity of the pulsar halo is always fixed at  $L_{\rm ref}$ . The resulting values of  $\xi$  are displayed in the four panels of Figure 3.

We see that mirage sources are commonly expected for nearby sources, i.e.,  $d < 1 \,\mathrm{kpc}$ . For more distant sources, the value of  $\xi$  declines significantly with increasing distance d. The decline can be attributed to the blurring effect of the PSF, and to the reduction in the signal-to-noise ratio at greater distances. Above  $4 \,\mathrm{kpc}$ , we almost do not expect any mirage source around the accelerator. In addition to such a general trend, we see that the mirage ratio between  $1.5-3.5 \,\mathrm{kpc}$  also depends on various

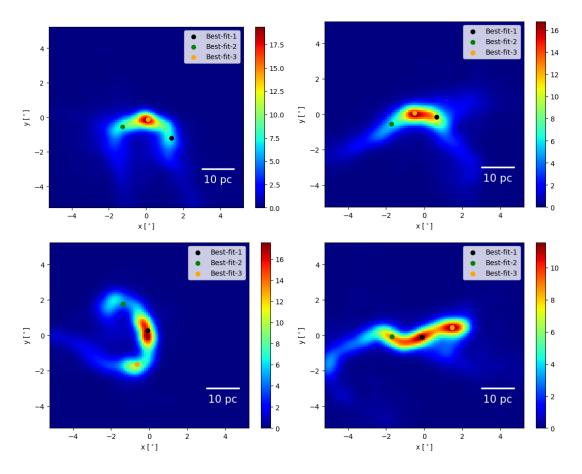


FIG. 1. Four sets of mirages sources (with distance at 250 pc). The color shows the relative intensity. The electrons are injected at (0,0), and the black, green and orange dots show the detected source locations.

## model parameters.

We explore the influence of the coherence length in the top-left panel. As  $L_{\rm c}$  increase, the value of  $\xi$  increases significantly. The underlying reason is that a longer coherence length leads to a greater separation between two mirage sources and hence less influence by the PSF, as will be explained subsequently. If the coherence length is small, electrons can cross multiple coherence magnetic fields before cooling, so their distribution becomes largely isotropic and hence do not produce an enhancement of electron column density toward certain directions. The injection spectral index also affects the mirage ratio but not as strongly as  $L_c$  does, as shown in the top-right panel.  $\xi$  rises for a steeper spectrum (larger  $\alpha$ ). This can be explained as follows: particles with larger energies propagate more isotropically [21], and a smaller  $\alpha$  implies that more particles were injected earlier (and cooled down from a higher energy), and therefore propagate more isotropically.  $\xi$  also increases slightly as  $B_{\rm r}/B_{\rm t}$  rises. This is intuitive because when  $B_{\rm r}/B_{\rm t}$  is larger (and the total magnetic field energy remains the same), less energy is deposited in the turbulent energy, and the transport is closer to that in the anisotropic diffusion scenario [14], preferentially resulting in an elongated

source with a gradually varying 2D intensity map. Meanwhile,  $\xi$  decreases as  $B^2$  increases, because the distance on which particles are transported depends on their energy losses, which are more severe when the magnetic field is stronger, and it then becomes harder for the separation of the sources to overcome the PSF. Comparing the cases of  $B^2 = 9\mu G^2$  and  $81\mu G^2$ , the impact of  $B^2$  is relatively weak because when the magnetic field is weak, the energy losses are dominated by the IC losses, the energy density of which is equivalently a magnetic field of  $\sim 3.6~\mu G$ .

## C. Source separation and flux ratio

In this subsection, we discuss the separation distance (defined as the maximal separation distance between any two sources if two or more mirage sources are identified) and the flux ratio ( $\chi$ , defined as main source/mirage source, where the main source is the source with the smallest distance to the injection point and the mirage source is the farthest one) of the sources. For each chosen set of parameters, we carry out 100 runs and calculate the above two quantities of each run, and show their distribu-

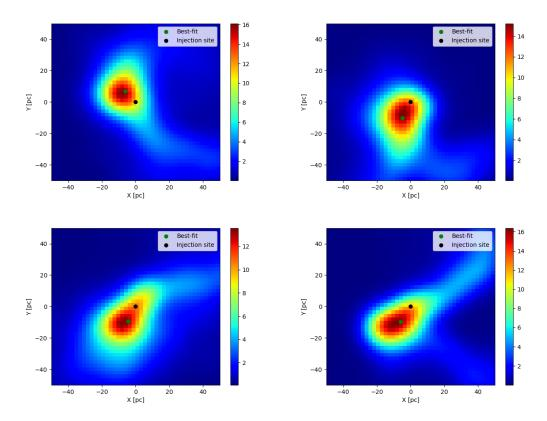


FIG. 2. Four sets of large offsets (with distance at 1 kpc). The color shows the relative intensity. The black dots show the electron injection site locations, and the green dots correspond to the detected source locations.

tion in the plane of separation value and flux ratio. In all runs, the accelerator's distance is fixed at  $d=1\,\mathrm{kpc}$ . To reveal the difference more clearly, we set here a higher criterion TS= 25 for the identification of a source. As such, the mirage ratio will decrease compared to the case shown in Figure 3 with the same parameters (i.e., not all runs can generate a mirage source at  $d=1\,\mathrm{kpc}$ ).

Our results are shown in Figure 4. In the top panel of the figure, we can see that the mean separation between the main source and the mirage source is positively correlated with  $L_{\rm c}$ . Given that the mirage source is formed due to the projection effect when particles propagate to another coherence of the magnetic field as discussed before, the separation value is correlated with the coherence length. On the other hand, we do not see a clear dependence of the flux ratio  $\xi$  on  $L_{\rm c}$ .

The influence of the magnetic field strength is noticeable on both the separation value and the flux ratio, as shown in the middle panel of Figure 4. The effect can be attributed to faster cooling of electrons in stronger magnetic fields. Injected electrons may not cross one coherence length before cooling if the magnetic field strength is strong, and therefore only reveal the small bents within one coherence length of the magnetic field, leading to a smaller separation between the main source and the mirage source. Due to the same reason, the electron number consisting of the mirage source is also smaller for

a stronger magnetic field, leading to a lower flux ratio. From the middle panel of Figure 4, we see that the flux of the mirage source may be larger than the main source in a considerable fraction of runs with  $B^2=1$  and  $9\,\mu\text{G}^2$ . For  $B^2=81\,\mu\text{G}^2$ , the flux ratio is greater than unity in most of runs.

The regular-to-turbulent ratio  $B_{\rm r}/B_{\rm t}$  also affects the source separation, although the impact is less important than the previous two parameters. We see from the bottom panel of Figure 4 that, when  $B_{\rm r}/B_{\rm t}$  decreases, the separation distance (statistically) increases slightly. Adding a regular magnetic field is equivalent to adding a wave of infinitely long wavelength. As this regular component becomes stronger, the coherence becomes less distinct. Correspondingly, there will be less significant change of the mean field direction. In this sense, it is similar to the influence of the coherence length. Indeed, in the extreme case of  $B_{\rm r}/B_{\rm t} \to \infty$ , electrons just spiral around the regular magnetic field, so no mirage source and subsequently no source separation is expected.

## D. Offsets

Now we investigate the spatial offsets of the identified sources from the accelerator. We locate the source at a relatively large distance, 6 kpc, to reduce the mirage

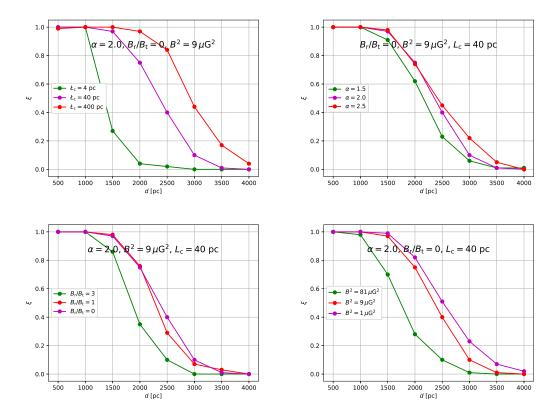


FIG. 3. Dependence of  $\xi$  on other parameters.

ratio, so that the definition of the offset is clear. Nevertheless, if more than one sources are identified, the offset is defined as the distance between the accelerator and the source closest to it.

For  $L = L_{ref}$ , as shown in the left columns of Figure 5, there are only a few points sparsely distributed in the plane of the offset and the total counts of the source (as a representative of the source flux). This is owing to the large distance we chose, which results in a low flux of the source and hence not many of them are identified. For those with a source being identified, the obtained offsets are quite large for  $L = L_{ref}$ . This is because when the source is faint and the distance is far, the position of the Gaussian centre is subject to the noise fluctuation and large PSF. If we assume a higher lumionsity, i.e.,  $L = 10L_{\rm ref}$ , as shown in the right column of Figure 5, the offsets become generally smaller. Meanwhile, as can be expected, the offset increases with larger  $L_c$  and is inversely correlated to  $B^2$ . The reasons are similar to that for the separation distance, as discussed in the last section.

The  $\gamma$ -ray luminosity  $\mathcal{L}$  of the source has an impact on source identification. This can be seen in the count maps displayed in Figure 6 and in Figure 7. The former shows a configuration of the turbulence with  $L_{\rm c}=400$  pc, and the latter another configuration with  $L_{\rm c}=4$  pc. In the configuration with  $L_{\rm c}=400$  pc, the emission is found to be identified as two sources when the luminosity is equal

to  $10\mathcal{L}_{\mathrm{ref}}$  (see the left panel in Figure 6), while it can only be identified as one source when it is equal to  $\mathcal{L}_{\mathrm{ref}}$  (see the right panel). In the configuration with  $L_{\mathrm{c}}=4$  pc, the centre of the emission is not affected by the noise when the luminosity is set to  $10\mathcal{L}_{\mathrm{ref}}$  (see the left panel in Figure 7), while it is strongly affected by the noise when it is set to  $\mathcal{L}_{\mathrm{ref}}$  (see the right panel).

### IV. POSSIBLE APPLICATIONS

In the LHAASO catalog [18], some sources have been discovered in the vicinity of middle-aged pulsars, but the centres of these sources show significant offsets from the positions of the pulsars. See in particular those listed in Table I. These offsets may be linked with the mirage halo phenomenon discussed here. We checked this possibility by simulating particle propagation around these pulsars, based on the Jansson-Farrar model of the Galactic magnetic field [30, 31]. This model provides the interstellar magnetic field strength, and the ratio between the regular and the turbulent magnetic field strengths at the position of each pulsar, which are important parameters in our simulations as discussed in the previous Section. We note that the turbulence level in this model needs be re-scaled by a factor  $\beta$  to fit the boron-to-carbon ratio (B/C) [22, 32]. We find that  $\beta = 0.27$  gives a rea-

TABLE I. Possible applicable sources

Source name	PSR name	Gl	$\operatorname{Gb}$	Distance (kpc)	$B_{\rm r} \; (\mu {\rm G})$	$B_{\rm t} \; (\mu {\rm G}, \; \beta = 0.27)$	Offset (pc)	Offset $(^{\circ})$	ζ
1LHAASO J0216+4237u	J0218+4232	139.508	-17.527	3.150	0.89	0.52	18.14	0.33	41%
1LHAASO J1837-0654u	J1838-0655	25.246	-0.196	6.600	1.35	2.28	13.82	0.12	26%
1LHAASO J1912+1014u	J1913+1011	44.485	-0.167	4.613	0.62	8.65	10.47	0.13	12%
1LHAASO J2005+3415	J2004+3429	71.425	1.571	10.783	0.25	0.85	47.05	0.25	84%
1LHAASO J2005+3050	J2006+3102	68.667	-0.530	6.035	0.27	1.85	21.07	0.20	10%

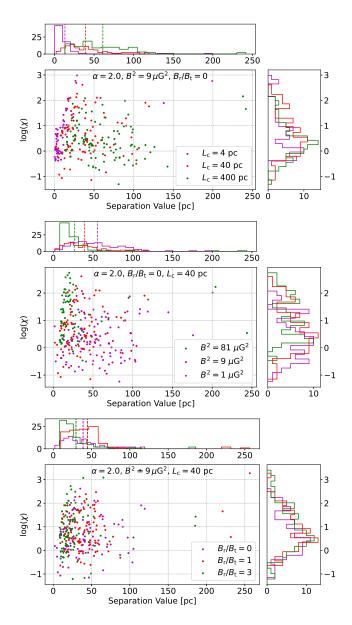


FIG. 4. Scatter plot of the flux ratio  $\chi$  and separation distance for different  $L_{\rm c}$  (top panel), magnetic field strength  $B^2$  (middle panel) and the strength ratio between regular field and turbulent field  $B_r/B_t$  (bottom panel). The distance is fixed at 1 kpc. The dashed line in the histogram mark the average value of the separation.

sonable residence time of cosmic rays in our Galaxy by performing the same simulation as presented in Ref.[32], so that the predicted cosmic-ray grammage [33] is consistent with the cosmic-ray B/C measurement of AMS-02 [34]. In the simulation, we employ  $L_c=220\,\mathrm{pc}$  following the observation of the power spectrum of Galactic foreground rotation-measure maps [22]. For a smaller coherence length,  $\beta$  could be smaller, but still at the level of  $\sim 0.1$ , see Ref. [32].

Then, we further assume an injection spectral index  $\alpha = 2$  for the electrons, and we simulate electron propagation around each of the pulsars that are mentioned above. To reduce the influence of the randomly generated turbulence on the results, we perform 100 separate runs of simulations for each pulsar and calculate the offset generated in each run. A threshold TS value of 49 (as is used in the LHAASO catalog), rather than 25, is used for source identification. The possibility of explaining the offsets with mirage halos is evaluated with  $\zeta$ , which is defined as the fraction of the runs showing a source offset larger than the observed one. The obtained values of  $\zeta$  are shown in the last column of Table I. We can see that relatively weak regular magnetic fields are present in the ISM around these pulsars, which is in favor of producing mirage halos. Indeed, the probability of showing large offsets are found to be above 10% for all the listed pulsars, demonstrating that mirage halos may be a reasonable explanation for these measured large offsets.

### V. SUMMARY AND DISCUSSION

Propagation of high-energy cosmic rays in the ISM close to their accelerators plays an important role in shaping the morphology of extended gamma-ray sources. In the companion paper [23], we found that the propagation of electrons is highly asymmetric, and that this may lead to the appearance of so-called mirage halos, as well as significant spatial offsets between the positions of the measured gamma-ray sources and that of their parent accelerators. In the present paper, we explored in detail the formation mechanism of these mirage halos and spatial offsets, and we investigated quantitatively the influence of the model parameters on the appearance of these two phenomena.

We performed test-particle simulations of the propagation of electrons above 100 TeV in the interstellar magnetic fields around their accelerators, taking radia-

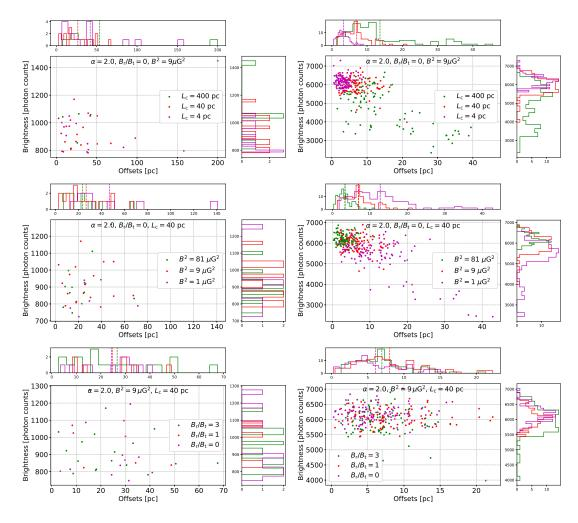


FIG. 5. Scatter plot of offsets and total counts of the identified source which is closest to the accelerator for different  $L_c$  (top panels),  $B^2$  (middle panels), and  $B_r/B_t$  (bottom panels). The distance is fixed at 6 kpc (the pixel size 0.1° corresponding to  $\approx 10$  pc; the PSF (0.3°) corresponding to  $\approx 30$  pc). In the left columns, the luminosity is  $\mathcal{L} = \mathcal{L}_{ref}$ , while in the right columns, the luminosity is  $\mathcal{L} = 10\mathcal{L}_{ref}$ . Dashed lines in the histogram mark the average value of the offset.

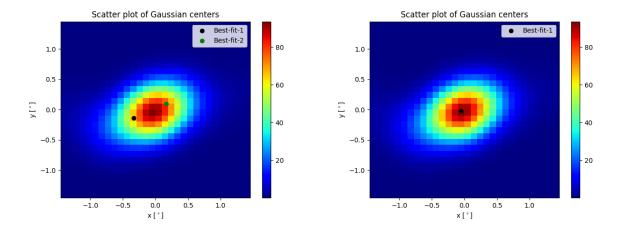


FIG. 6. The counts map (relative intensity) for one configuration with  $L_{\rm c}=400$  pc and distance of 6 kpc. The emission can be identified as two sources if the  $\gamma$ -ray luminosity is  $\mathcal{L}=10\mathcal{L}_{\rm ref}$  (left panel), and it can only be identified as one source when  $\mathcal{L}=\mathcal{L}_{\rm ref}$  (right panel). The noise has been removed.

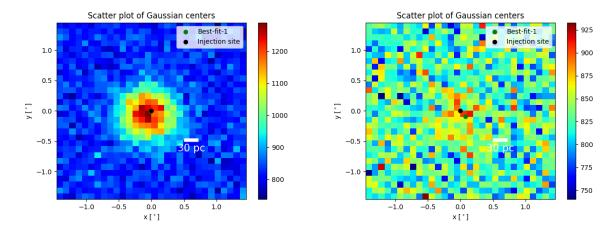


FIG. 7. The counts map (absolute counts number) for one configuration with  $L_c = 4$  pc. The centre of the emission is not affected by the noise when  $\mathcal{L} = 10\mathcal{L}_{ref}$  (left panel), and it is severely affected by the noise when  $\mathcal{L} = \mathcal{L}_{ref}$  (right panel). The noise is kept.

tive cooling into account. With the obtained distributions of electrons, we then calculated their IC radiation and obtained the mock count maps as would be seen by LHAASO, as well as the identifiable sources following the standard likelihood analysis. We found that the mirage sources and the large spatial offsets between identified sources and particle accelerators can be ascribed to the asymmetric propagation of particles in the magnetic field and to projection effects. More specifically, particles propagate preferentially along the direction of their local magnetic field lines, which changes dramatically between two coherence lengths. If the field line within a certain magnetic coherence length is approximately aligned with our line of sight, an apparent enhancement of the electron column density appears in our direction due to a projection effect. A mirage source or a source offset is then created.

Furthermore, based on the properties of identified sources, the influence of model parameters on the propagation of electrons have been evaluated with three indicators, namely, the mirage ratio, the maximum separation distance, and the offset. The mirage ratio is the proportion of runs with identification of two or more sources, and the maximum separation distance is the maximum distance between any two sources identified in one run. The offset is the distance between the pulsar's position and the centroid of the closest identified source. Our main findings include:

- The mirage ratio is negatively correlated with d,  $B_{\rm r}/B_{\rm t}$  and  $B^2$ , and is positively correlated with  $L_{\rm c}$  (strong dependence) and  $\alpha$  (weak dependence). The mirage ratio is almost 100% at 1 kpc with the reference  $\gamma$ -ray luminosity. Even at a distance of 3 kpc, the mirage ratio could still reach more than 10% with reasonable combinations of parameters.
- The maximum separation is negatively correlated with  $B^2$ , and positively correlated with  $L_c$ . The

large maximum separation suggests that in the inter-arm region, and in the Galactic halo (where the coherence length is larger), two sources separated with 100 pc could still be linked with one another and belong to the same halo.

• The offset is also negatively correlated with  $B^2$ , and positively correlated with  $L_c$ . Our calculations suggest that in the inter-arm region, and in the Galactic halo (where the coherence length is larger), the offsets between pulsar and the halo centroid could be as large as 50 pc.

We have also discussed the possible application of this mechanism to explain some LHAASO sources with pulsar associations. For example, 1LHAASO J0216+4237u, J0212+4254u, and J0206+4302u could have a common origin, and be explained as mirage halos powered by the millisecond pulsar PSR J0218+4232. The large offsets between a few middle-aged pulsars and LHAASO sources may also be explained by our model naturally.

In our simulations, we do not consider the feedback of relativistic particles on the magnetic field, such as the streaming instability. This simplification is reasonable for energetic electrons ( $>100\,\mathrm{TeV}$ ), because the energy density of such high-energy electrons is usually very small compared with that of the interstellar medium, and hence the growth of such instabilities should be very slow.

We also note that the synthetic turbulent magnetic fields used in our simulations are generated following Ref. [24], assuming an isotropic turbulence with Kolmogorov-type power spectrum. The nature of the turbulence in the interstellar medium may display some differences. In particular, studies have shown that Alfvénic turbulence is highly anisotropic at the gyro-scale of cosmic rays and thereby inefficient at scattering cosmic rays, while fast modes are isotropic and should play a dominant role in scattering cosmic rays [35], as supported

by the recent analysis of radio polarisation observations [36]. Therefore, some differences must exist between the cosmic-ray scattering rates for particles propagating in our synthetic turbulence and that for particles propagating in magnetohydrodynamic turbulence. Although our synthetic turbulence may not be accurate on the cosmic-ray gyration scales, it still qualitatively captures the isotropic and filamentary nature of the interstellar turbulence on large scales, which is due to modes with large wavelengths. These modes are actually those which drive the filamentary propagation of cosmic-rays along magnetic field lines and thereby the formation of asymmetric gamma-ray emissions [21], mirage sources, and large offsets. Therefore, our calculations provide a reasonably good approximation of realistic interstellar turbulence, for the study of the appearance of asymmetric extended gamma-ray emissions around cosmic-ray

sources. Furthermore, this method can take into account a wide range of length scales in the turbulence from the gyroradius of relevant electrons up to the turbulence injection scale with reasonable computing times. More realistic simulations, such as particle-in-cell simulations, or particle propagation in 3D cubes from magnetohydrodynamic simulations can, however, only cover a limited range of spatial scales, limiting the ranges of electron energies that can be studied with them.

#### ACKNOWLEDGMENTS

We thank Chunkai Yu, Hao Zhou and Giovanni Morlino for discussion. This work is supported by NSFC under grants No. 12393852, 12350610239, 12393853, 12173018, 12121003, and U2031105.

- [1] L. Sironi and A. Spitkovsky, ApJL 783, L21 (2014), 1401.5471.
- [2] B. Cerutti, A. A. Philippov, and G. Dubus, Astronomy and Astrophysics **642**, A204 (2020), 2008.11462.
- [3] Lhaaso Collaboration, Z. Cao, F. Aharonian, Q. An, Axikegu, L. X. Bai, Y. X. Bai, Y. W. Bao, D. Bastieri, X. J. Bi, et al., Science 373, 425 (2021), 2111.06545.
- [4] L. Sironi and A. Spitkovsky, Astrophys. J. 741, 39 (2011), 1107.0977.
- [5] B. Cerutti and A. A. Philippov, Astronomy and Astrophysics 607, A134 (2017), 1710.07320.
- [6] G. Giacinti and J. G. Kirk, Astrophys. J. 863, 18 (2018), 1804.05056.
- [7] B. Cerutti and G. Giacinti, Astronomy and Astrophysics 642, A123 (2020), 2008.07253.
- [8] A. U. Abeysekara, A. Albert, R. Alfaro, C. Alvarez, J. D. Álvarez, R. Arceo, J. C. Arteaga-Velázquez, D. Avila Rojas, H. A. Ayala Solares, A. S. Barber, et al., Science 358, 911 (2017), 1711.06223.
- [9] F. Aharonian, Q. An, L. X. Axikegu, Bai, Y. X. Bai, Y. W. Bao, D. Bastieri, X. J. Bi, Y. J. Bi, H. Cai, J. T. Cai, et al., Phys. Rev. Lett. 126, 241103 (2021), 2106.09396.
- [10] C. Evoli, T. Linden, and G. Morlino, Phys. Rev. D 98, 063017 (2018), 1807.09263.
- [11] K. Fang, X.-J. Bi, and P.-F. Yin, Mon. Not. R. Astron. Soc. 488, 4074 (2019), 1903.06421.
- [12] P. Mukhopadhyay and T. Linden, Phys. Rev. D 105, 123008 (2022), 2111.01143.
- [13] R. López-Coto and G. Giacinti, Mon. Not. R. Astron. Soc. 479, 4526 (2018), 1712.04373.
- [14] R.-Y. Liu, H. Yan, and H. Zhang, Phys. Rev. Lett. 123, 221103 (2019), 1904.11536.
- [15] B. Schroer, C. Evoli, and P. Blasi, Phys. Rev. D 107, 123020 (2023), 2305.08019.
- [16] T. Linden, K. Auchettl, J. Bramante, I. Cholis, K. Fang, D. Hooper, T. Karwal, and S. W. Li, Phys. Rev. D 96, 103016 (2017), 1703.09704.
- [17] T. Sudoh, T. Linden, and J. F. Beacom, Phys. Rev. D 100, 043016 (2019), 1902.08203.
- [18] Z. Cao, F. Aharonian, Q. An, Axikegu, Y. X. Bai, Y. W.

- Bao, D. Bastieri, X. J. Bi, Y. J. Bi, J. T. Cai, et al., ApJS **271**, 25 (2024), 2305.17030.
- [19] A. Albert, R. Alfaro, C. Alvarez, J. R. A. Camacho, J. C. Arteaga-Velázquez, K. P. Arunbabu, D. Avila Rojas, H. A. Ayala Solares, V. Baghmanyan, E. Belmont-Moreno, et al., Astrophys. J. 905, 76 (2020), 2007.08582.
- [20] Y. Zhang, R.-Y. Liu, S. Z. Chen, and X.-Y. Wang, Astrophys. J. 922, 130 (2021), 2010.15731.
- [21] G. Giacinti, M. Kachelrieß, and D. V. Semikoz, Phys. Rev. Lett. 108, 261101 (2012), 1204.1271.
- [22] M. C. Beck, A. M. Beck, R. Beck, K. Dolag, A. W. Strong, and P. Nielaba, JCAP 2016, 056 (2016), 1409.5120.
- [23] Y. Bao, G. Giacinti, R. Liu, H. Zhang, and Y. Chen, Phys. Rev. Lett., submitted (2024).
- [24] J. Giacalone and J. R. Jokipii, Astrophys. J. 520, 204 (1999).
- [25] D. DeMarco, P. Blasi, and T. Stanev, JCAP 2007, 027 (2007), 0705.1972.
- [26] G. Giacinti, M. Kachelrieß, D. V. Semikoz, and G. Sigl, JCAP 2012, 031 (2012), 1112.5599.
- [27] K. Fang, X.-J. Bi, S.-J. Lin, and Q. Yuan, Chinese Physics Letters 38, 039801 (2021), 2007.15601.
- [28] S. Zenitani and T. Umeda, Physics of Plasmas 25, 112110 (2018), 1809.04378.
- [29] F. Aharonian, Q. An, Axikegu, L. X. Bai, Y. X. Bai, Y. W. Bao, D. Bastieri, X. J. Bi, Y. J. Bi, H. Cai, et al., Chinese Physics C 45, 025002 (2021), 2010.06205.
- [30] R. Jansson and G. R. Farrar, Astrophys. J. 757, 14 (2012), 1204.3662.
- [31] R. Jansson and G. R. Farrar, ApJL 761, L11 (2012), 1210.7820.
- [32] G. Giacinti, M. Kachelrieß, and D. V. Semikoz, Phys. Rev. D 91, 083009 (2015), 1502.01608.
- [33] Note1, the cosmic-ray grammage is given by  $\langle X \rangle = 1.4 m_{\rm p} n_{\rm p} \langle t_{\rm res} \rangle c$ , where  $t_{\rm res}$  is the residence time,  $n_{\rm p}$  is the hydrogen density in the ISM,  $m_p$  is the mass of proton, and the prefactor 1.4 takes into account the contribution of nuclei (such as helium) in the ISM.
- [34] M. Aguilar, L. Ali Cavasonza, B. Alpat, G. Ambrosi, L. Arruda, N. Attig, C. Bagwell, F. Barao, L. Barrin,

- A. Bartoloni, et al., Phys. Rev. Lett. **130**, 211002 (2023). [35] H. Yan and A. Lazarian, Phys. Rev. Lett. **89**, 281102 (2002), astro-ph/0205285.
- [36] S. Malik, K. H. Yuen, and H. Yan, Astrophys. J. 965, 65 (2024), 2307.13342.